Chapter 5

Computational analysis of dendritic signal integration

5.1 Export of neuronal geometry into computational modelling software and data visualization

Precise neuronal geometric reconstructions enable the theoretical analysis of neuronal signal integration in complex dendritic trees by multi-compartment modelling, and therefore help to understand the functional consequences of neuronal architecture for computation within individual neurons. In a first step however it is required to transport the data describing neuronal architecture into the proprietary format of modelling software such as NEURON or GENESIS. I therefore equipped the reconstruction software presented in chapter 2 and 3 with export routines, which directly generate geometric model descriptions. Furthermore, the definition of membrane conductance along neuronal sub-segments and point processes like synapses, and voltage and current monitors is supported by interactively browsing through 3-dimensional reconstructions within AMIRA software. Therefore, the plain preparation of geometric computational models is now possible without further need of coding the neuron's geometry in model description language. Theoretical neurobiologists are therefore left to exclusively concentrate on the programming of experimental paradigms.

Although NEURON and GENESIS come with methods to display modelling results in 3-dimensions, the user interactivity is restricted. Extensive graphical interaction possibilities ease the intellectual comprehension of theoretical modelling and accelerate data evaluation. To integrate the elaborate modelling possibilities of NEURON and GENESIS with sophisticated 3-dimensional display and interaction possibilities, I have written

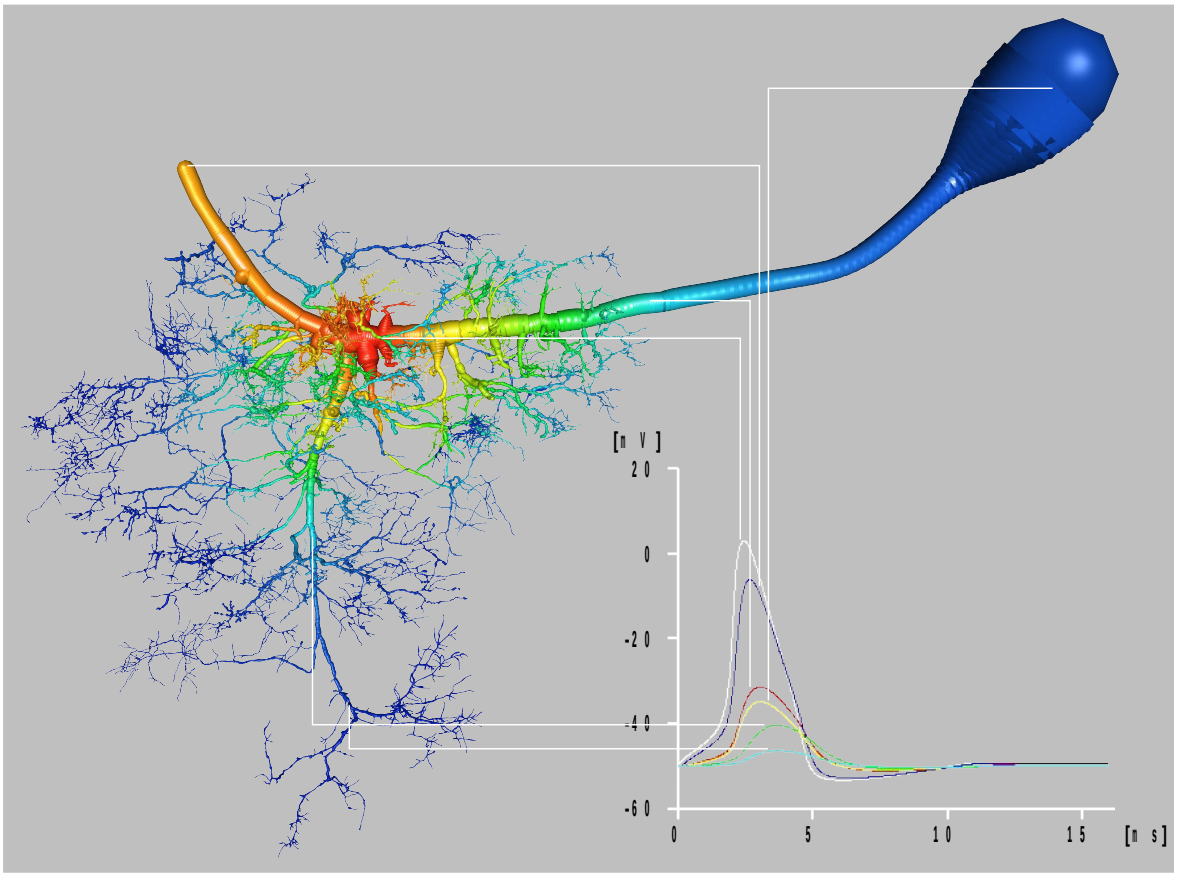

Figure 5.1: Interactive evaluation and visualization of computational modelling results. Routines were developed in the scripting language of respective modelling programs to transfer modelling data into the custom-written reconstruction and visualization programs (described in chapter 2 and 3). This is demonstrated for a geometric reconstruction of the MN5 at pupal stage 5. The passive spread of an action potential in the dendritic tree is shown false-color coded, as exemplarily determined by computational modelling. Voltage traces of selected individual compartments are plotted to the right of the reconstruction. Membrane properties and point processes (such as synapses or current/voltage monitors) can be interactively defined within AMIRA and exported into the native modelling description language of both, NEURON and GENESIS.

routines to import modelling data back into Amira program environment (Fig. 5.1). These methods now allow a streamlined generation and visualization for computational modelling experiments.

5.2 Parameter search for passive membrane properties

I have used these tools to generate geometric compartment models of the dendritic field of the MN5 of *Manduca sexta* at different developmental stages. To equip these models

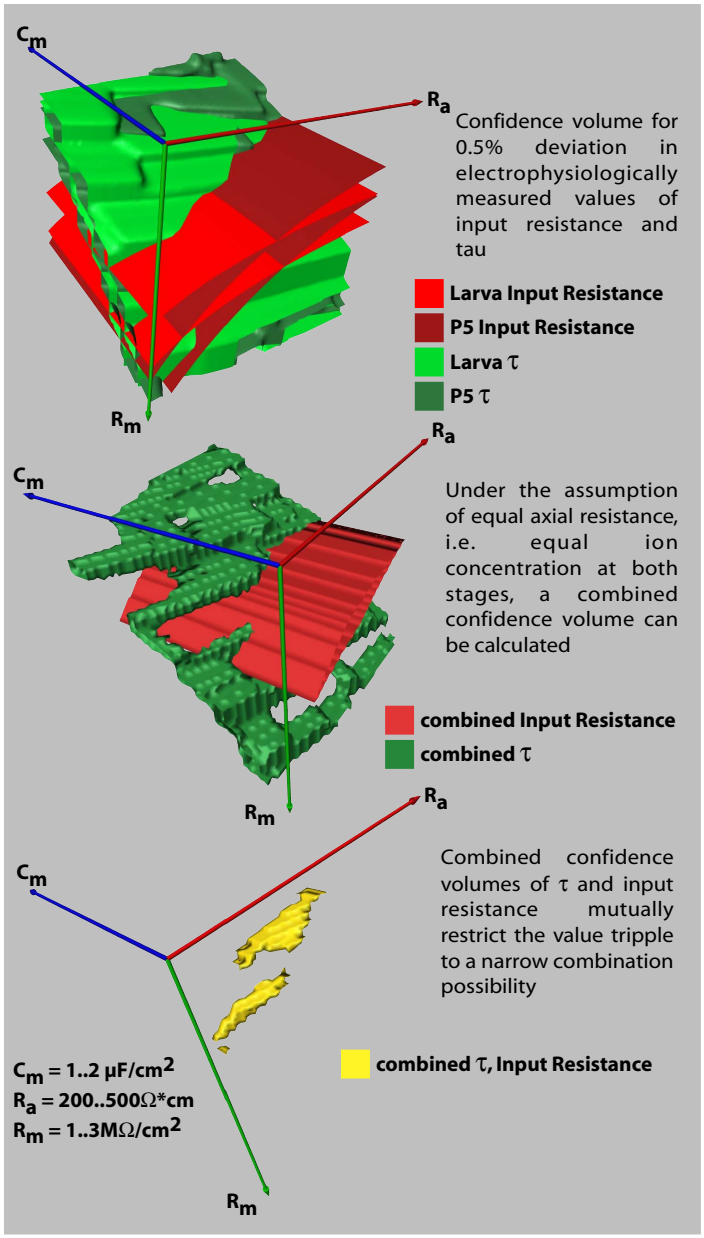

Figure 5.2: Parameter search for passive neuronal properties. Input resistance (R_i) and time constant (τ) can be determined from single electrode recordings of different neuronal morphologies at the cell body. To generate respective R_i and τ in multicompartment models of the corresponding neuronal geomerties, appropriate values of specific membrane resistance (R_m), specific axio-plasmatic resistance (R_a) and specific membrane capacity (C_m) must be determined. The top panel shows the planes in the 3-dimensional space of R_a, R_m and C_m which include the possible parameter combinations for the lower and upper confidence interval of two different morphologies, namely the MN5 of larval stage 5 and pupal stage 5. Under the assumption of equal R_a, the individual value spaces of both morphologies can be intersected, which effectively narrows the possible value combinations (mid panel). Further reduction of the parameter space is achieved by intersecting the value spaces for τ and R_i (bottom panel).

with realistic passive properties, three parameters must be determined: axoplasmatic resistance (R_a), specific membrane resistance (R_m) and specific membrane capacity (C_m). These variables can not be directly measured in living systems and must be inferred from electrophysiological data. The best way is to patch onto a dendritic tree at two separate places and measure the signal filtering properties of the neuronal tree, described by time constant (τ), length constant (λ) and effective input resistance (R_i). Together with a known dendritic geometry, these measures can then be used to analytically determine R_a, R_m and C_m for every compartment (Rall, 1969a,b). Impaling single neurons with two electrodes is a very demanding task and has been established in very few systems

only. Therefore, in a third step, I developed a computational modelling approach to estimate the passive neuronal properties with electrophysiological recordings from single electrode measurements (Fig. 5.2). The parameter space of R_a, R_m and C_m is sampled to determine the continuous plane of value-triples which generate R_i and τ as measured with one electrode (Fig. 5.2*A*). The 3 axis represent C_m, R_m, R_a. The red planes represent the parameter spaces deducted from measured input resistance data. The green planes represent the parameter spaces deducted from measured time constant. The resulting section line of planes is the only analytic solution of possible value triples. Applying this procedure on two distinct neuronal morphologies, for instance at two different stages such as larval stage 5 and pupal stage 5, two sets of possible value triples can be determined. The parameter space can be further decreased under the plausible assumption of equal ionic composition of the axoplasmatic medium of both neurons (this assumption is also used in all patch clamp studies because they use the same intracellular ionic solution for all stages): R_a must be identical and only C_m and R_m can be varied. Therefore, the intersection of parameter spaces from different morphologies can be calculated, which further confines the allowed parameter space to be even smaller.
Because measuring data from living cells underlies certain variability, the above described planes of possible value triples become spaces, and therefore also section-lines become section-spaces (Fig. 5.2*B*). Further combining value spaces for input resistance and time constant, the resulting space for value triples of R_a, R_m and C_m is an effectively analytically narrowed selection of value triples (Fig. 5.2*C*). I have applied this method successfully using larval and pupal stage 5 geometric reconstructions, which yielded values for R_m ($\sim$1.5MΩ/cm^2), R_a ($\sim$350 $\Omega\times$cm) and C_m ($\sim$1.3μF/cm^2) which are in the range commonly applied values in computational models of other neurons.

5.3 Does postembryonic remodelling of MN5's dendritic geometry support its altered behavior?

Having determined the passive neuronal properties for MN5 sets the stage for multicompartment modelling. The slow larval MN5 integrates volleys of synaptic potentials and answers with tonic depolarization and bursts of action potentials to induce graded muscle contraction. In contrast to that, the adult MN5 has to fire precisely timed action potentials at about every 30 milliseconds ($\sim$30 Hertz), whereas every single action potential evokes a full power twitch of the respective flight muscle bundle. To generate stable flight, the muscle bundle must contract synchronously with the other 4 portions of the

DLM. Therefore, the remodelling of dendritic architecture of the MN5 during metamorphosis is ideal for investigating whether the MN5's quite opposite larval and adult behavioral demands on neuronal computation are met by a co-operative structure-function interrelation. I began to tackle this question by conducting the following experimental designs:

1. Is there a functional difference for dendritic computation between a fixed number of randomly distributed synapses and a distribution derived from the localization analysis of immuno-histochemically stained presynaptic profiles ((Evers et al., 2005), see Chapter 3)? One way to address this question was to let synapses fire with variable synchronicity and determine the timing dependent statistic distribution of the resulting membrane voltage. The time course and maximum value of the induced voltage deflection at the root of the dendritic tree was recorded. One hypothesis was that a synapse distribution derived from immuno-histochemical analysis might be optimized to reach a maximum depolarization within shortest time in adult neurons, not much affected by slight asynchronicity. The larval synapse distribution might be optimized to induce a long lasting depolarization which is more affected by asynchronous synaptic input. These experiments were computationally very expensive, and therefore, only the first part was finished: analysis of the effects of varied synchronicity of synaptic input for multiple total numbers of synapses for the larval (Fig. 5.3*A*) and pupal stage 5 (Fig. 5.3*B*) dendritic trees. The immuno-histochemically derived distribution of synapses (blue spheres) is depicted along the dendritic reconstruction (yellow). The larval stage dendritic tree needed more synapses firing at higher synchronicity to reach equal maximum membrane potential as compared to the pupal stage 5 dendritic tree. The inset shows an exemplary synapse activation plot for a gauss distribution with a synchronicity of σ=0.02.

2. Are the reset properties of membrane depolarization after spike initiation affected by neuronal structure and does this support neuronal function? To ensure that the adult neuron starts integration of synaptic inputs at equal conditions (as we assume that central patterns generator flight motor output is equal from cycle to cycle), the geometry should be optimized to re-polarize after firing single spikes. In contrast, the larval neuron natively fires trains of action potentials riding on top of lasting membrane depolarization. I addressed this question in an indirect way, analyzing the maximum firing frequency which the respective neuron can achieve with a given equal ionic conductance composition of active membrane along the axon. Neurons

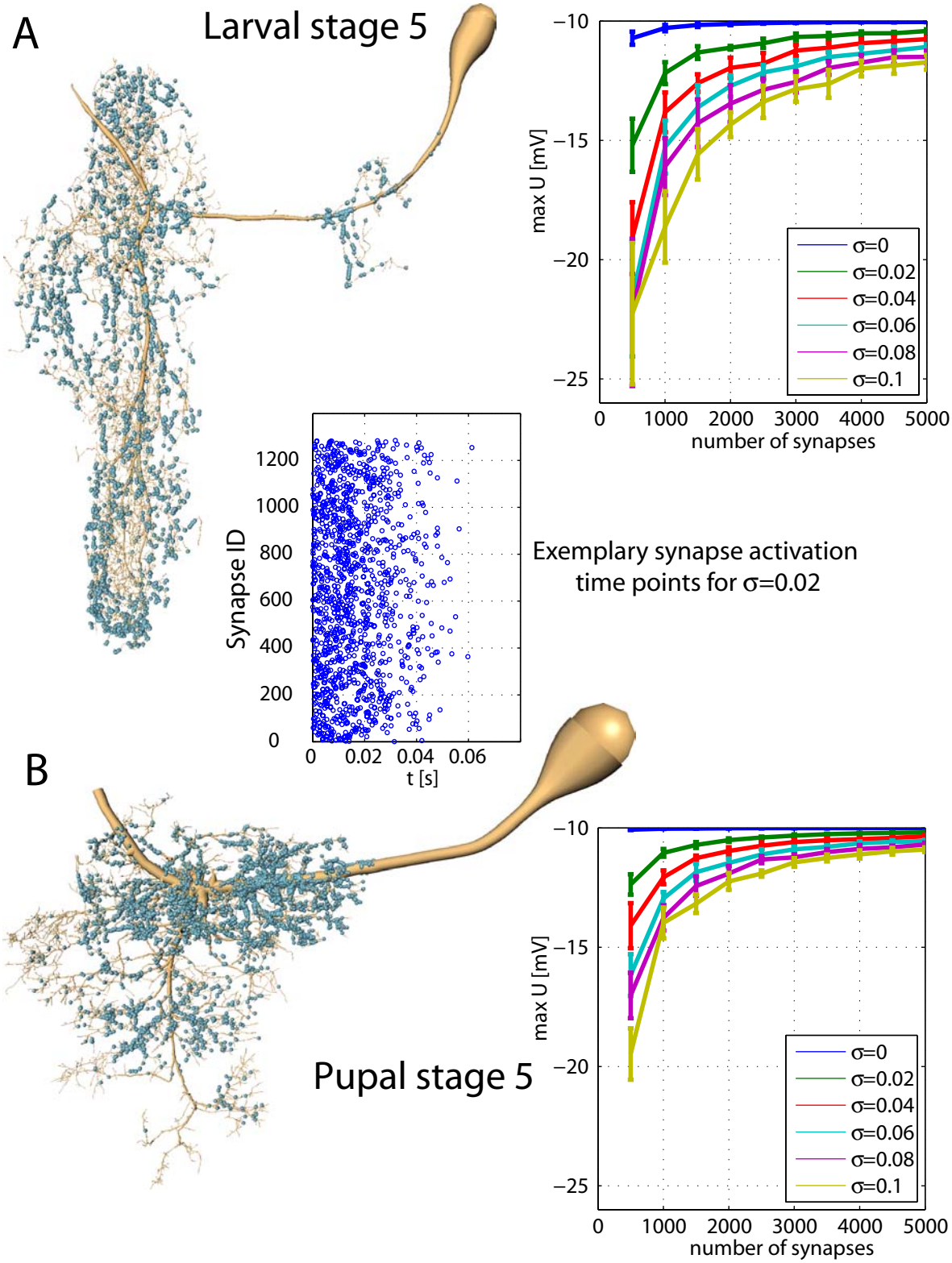

Figure 5.3: Developmental remodelling of dendritic architecture of MN5 alters its demand on synaptic synchronicity. Continued on next page.

Figure 5.3: continued

This is analyzed for a dendritic geometry of MN5 at both, larval stage 5 (A) and pupal stage 5 (B). Synapse localization (blue spheres) is derived from the distribution of immuno-labeled presynaptic profiles along MN5 dendritic projections (as described in chapter 3). The activation time point of individual synapses is drawn from Gaussian distributions. Different sigma values are used to generate different synaptic synchronicity (see inset for an exemplary synapse activation histogram at σ=0.02). The MN5 dendritic geometry at larval stage 5 (A) needs higher synchronicity of synaptic activation than that at pupal stage 5 (B) to induce an equal peak depolarization at the axo-dendritic junction. A lesser synapse quantity increases the dependency on synaptic synchronicity to induce maximum peak depolarization of membrane potential.

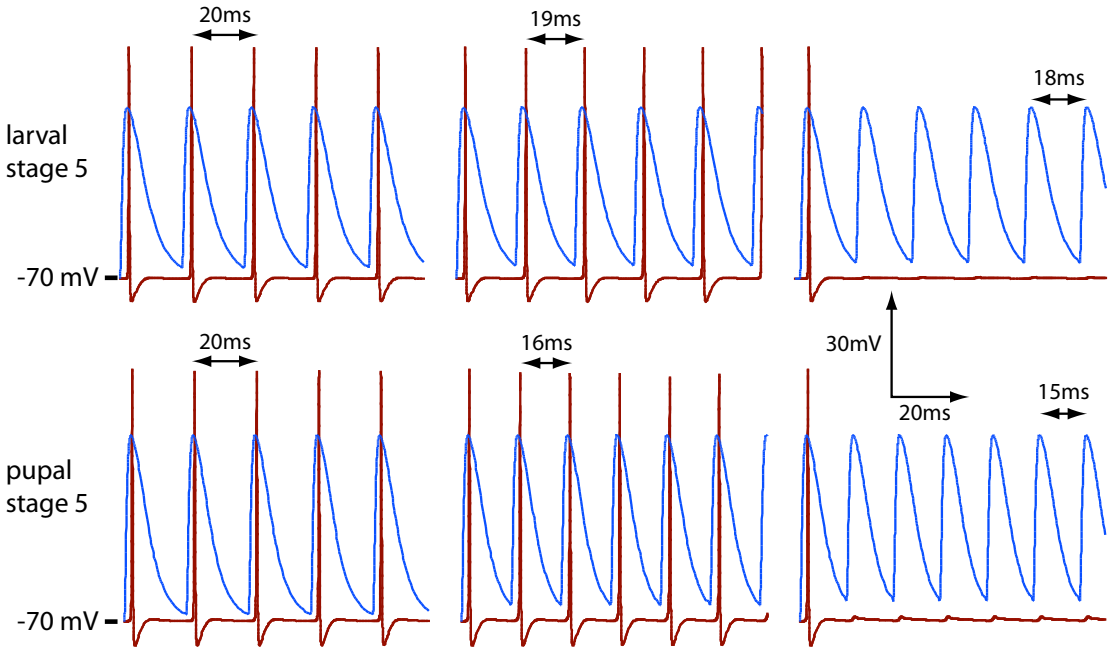

Figure 5.4: Cyclic synaptic activation can evoke action potential firing at higher frequencies in MN5 dendritic tree at pupal stage 5 than at larval stage 5. This is shown by equipping the geometric compartment models of MN5 at both stages with identical current densities with Hodgkin-Huxley kinetics at their axonal compartments. Dendrite compartments are defined to be purely passive (blue voltage trace at 40μm from axo-dendritic junction). Cyclic activation of synaptic conductance at every terminal dendrite ending is used to initiate the firing of single spikes at the axon (red trace). The pupal geometry supports the firing of action potentials at each synaptic activation interval as short as 16ms. In contrast, the laval geometry ceases to follow synaptic activation already at 18ms interval.

which are more effective in re-polarizing their dendritic tree should be able to fire higher frequencies upon synaptic stimulation. Therefore, the dendritic trees were equipped with synaptic conductance at all terminal endings of dendrites. The inter-stimulus delay was decreased from 20ms in 1ms steps. The results are plotted in Fig. 5.4 (red=axonal membrane depolarization; blue=dendritic voltage trace at 40μm distance from axo-dendritic junction). In larval stage 5, the inter-stimulus delay which repetitively evoked axonal action potentials was at 19ms. At 18ms inter-stimulus delay, the model neuron could not follow the stimulation anymore by firing action potentials. In contrast, in the model neuron of pupal stage 5, the neuron followed by firing action potentials up to an inter-stimulus time of 16ms but dropped the generation of action potential at 15ms inter-stimulus time. The data demonstrate that the geometry of the pupal stage 5 dendritic tree is better suited to follow high frequencies of synaptic stimulation, which might indicate functional co-operative structure for adult behavior.

These data, however, are gathered from models equipped with classic Hodgkin Huxley kinetics, which is surely inadequate for insect motorneurons (Heidel, personal communication). An additional problem is that MN5 at pupal stage 5 is not involved in the generation of motor behavior. Therefore, the comparison between the larval stage 5 MN5 and the pupal stage 5 MN5 is not adequate for comparing computational properties suitable for slow crawling versus fast flight behavior. A reconstruction of an adult dendritic tree is obviously needed, but has not yet been finished in sufficient detail to run computational models with it.

References

Evers, J. F., Schmitt, S., Sibila, M., and Duch, C. (2005). Progress in functional neuroanatomy: Precise automatic geometric reconstruction of neuronal morphology from confocal image stacks. *J. Neurophysiol.*, 93(4):2331–2342.

Rall, W. (1969a). Distributions of potential in cylindrical coordinates and time constants for a membrane cylinder. *Biophys J.*, 9(12):1509–41.

Rall, W. (1969b). Time constants and electrotonic length of membrane cylinders and neurons. *Biophys J.*, 9(12):1483–508.